



OGLE-2015-BLG-1771Lb: A Microlens Planet Orbiting an Ultracool Dwarf?

Xiangyu Zhang¹, Weicheng Zang¹ , Andrzej Udalski², Andrew Gould^{3,4}, Yoon-Hyun Ryu⁵ , Tianshu Wang^{1,6},
Hongjing Yang¹ , Shude Mao^{1,7}

(Leading Authors),

Przemek Mróz⁸ , Jan Skowron² , Radosław Poleski^{2,4}, Michał K. Szymański², Igor Soszyński² , Paweł Pietrukowicz² ,
Szymon Kozłowski² , Krzysztof Ulaczyk⁹

(THE OGLE COLLABORATION),

and

Michael D. Albrow¹⁰ , Sun-Ju Chung^{5,11} , Cheongho Han¹² , Kyu-Ha Hwang⁵ , Youn Kil Jung^{5,13} , In-Gu Shin⁵ ,
Yossi Shvartzvald¹⁴ , Jennifer C. Yee¹³ , Wei Zhu¹⁵ , Sang-Mok Cha^{5,16}, Dong-Jin Kim⁵, Hyoun-Woo Kim^{5,17},
Seung-Lee Kim^{5,11}, Chung-Uk Lee^{5,18}, Dong-Joo Lee⁵, Yongseok Lee^{5,16}, Byeong-Gon Park^{5,11}, and Richard W. Pogge⁴

(The KMTNet Collaboration)

¹ Department of Astronomy and Tsinghua Centre for Astrophysics, Tsinghua University, Beijing 100084, People's Republic of China
zangwc17@mails.tsinghua.edu.cn

² Warsaw University Observatory, Al. Ujazdowskie 4, 00-478 Warszawa, Poland

³ Max-Planck-Institute for Astronomy, Königstuhl 17, D-69117 Heidelberg, Germany

⁴ Department of Astronomy, Ohio State University, 140 W. 18th Avenue, Columbus, OH 43210, USA

⁵ Korea Astronomy and Space Science Institute, Daejeon 34055, Republic of Korea

⁶ Department of Astrophysical Sciences, Princeton University, USA

⁷ National Astronomical Observatories, Chinese Academy of Sciences, Beijing 100101, People's Republic of China

⁸ Division of Physics, Mathematics, and Astronomy, California Institute of Technology, Pasadena, CA 91125, USA

⁹ Department of Physics, University of Warwick, Gibbet Hill Road, Coventry, CV4 7AL, UK

¹⁰ University of Canterbury, Department of Physics and Astronomy, Private Bag 4800, Christchurch 8020, New Zealand

¹¹ Korea University of Science and Technology, 217 Gajeong-ro, Yuseong-gu, Daejeon 34113, Republic of Korea

¹² Department of Physics, Chungbuk National University, Cheongju 28644, Republic of Korea

¹³ Center for Astrophysics, Harvard & Smithsonian, 60 Garden Street, Cambridge, MA 02138, USA

¹⁴ Department of Particle Physics and Astrophysics, Weizmann Institute of Science, Rehovot 76100, Israel

¹⁵ Canadian Institute for Theoretical Astrophysics, University of Toronto, 60 St. George Street, Toronto, ON M5S 3H8, Canada

¹⁶ School of Space Research, Kyung Hee University, Yongin, Gyeonggi 17104, Republic of Korea

¹⁷ Department of Astronomy and Space Science, Chungbuk National University, Cheongju 28644, Republic of Korea

¹⁸ University of Science and Technology, Korea, (UST), 217 Gajeong-ro Yuseong-gu, Daejeon 34113, Republic of Korea

Received 2019 November 6; revised 2020 January 16; accepted 2020 January 17; published 2020 February 20

Abstract

We report the discovery and the analysis of the short ($t_E < 5$ days) planetary microlensing event, OGLE-2015-BLG-1771. The event was discovered by the Optical Gravitational Lensing Experiment, and the planetary anomaly (at $I \sim 19$) was captured by The Korea Microlensing Telescope Network. The event has three surviving planetary models that explain the observed light curves, with planet-host mass ratio $q \sim 5.4 \times 10^{-3}$, 4.5×10^{-3} and 4.5×10^{-2} , respectively. The first model is the best-fit model, while the second model is disfavored by $\Delta\chi^2 \sim 3$. The last model is strongly disfavored by $\Delta\chi^2 \sim 15$ but not ruled out. A Bayesian analysis using a Galactic model indicates that the first two models are probably composed of a Saturn-mass planet orbiting a late M dwarf, while the third one could consist of a super-Jovian planet and a mid-mass brown dwarf. The source-lens relative proper motion is $\mu_{\text{rel}} \sim 9 \text{ mas yr}^{-1}$, so the source and lens could be resolved by current adaptive-optics instruments in 2020 if the lens is luminous.

Unified Astronomy Thesaurus concepts: [Gravitational microlensing exoplanet detection \(2147\)](#)

Supporting material: data behind figure

1. Introduction

Early observations using ALMA (Testi et al. 2016) and *Herschel* (Daemgen et al. 2016) suggest that disks around brown dwarfs and M-dwarfs with mass below $0.1 M_\odot$ are frequent. Searching for and studying planets around such ultracool dwarfs ($M_{\text{host}} < 0.1 M_\odot$) are important for the conditions for planet formation theories (e.g., Ida & Lin 2005; Boss 2006) at the low-mass end. However, the detection of planets around ultracool dwarfs is challenging due to the

intrinsic faintness of the host stars. At the time of writing, more than 4000 confirmed exoplanets have been detected,¹⁹ but only 21 of them are orbiting an $M_{\text{host}} < 0.1 M_\odot$ star.

Among the 21 such known planets, four of them were found by direct imaging method: 2MASS 1207–3932 (Chauvin et al. 2004), 2MASS 0441–2301 (Todorov et al. 2010), VHS 1256–1257 (Gauza et al. 2015), and CFBDSIR 1458+1013 (Liu et al.

¹⁹ <http://exoplanetarchive.ipac.caltech.edu> as of 2019 October 31.

2011). All of these planets are super-Jovian planets ($>4 M_J$) and have a planet-host mass ratio $q > 0.15$, which indicates that these systems may form similarly to binary systems. In addition, seven temperate terrestrial planets were discovered around the nearby ultracool dwarf stars TRAPPIST-1 (Gillon et al. 2017) via the transit method, and two similar planets around Teegarden’s Star were detected by the radial velocity method (Zechmeister et al. 2019), which suggests that terrestrial planets should be frequent around ultracool dwarfs.

Microensing opens a powerful window for probing planets around ultracool dwarfs because it does not rely on the light from the host stars but rather uses the light from a background source (Mao & Paczynski 1991; Gould & Loeb 1992). Microensing has detected three planets orbiting an $M_{\text{host}} < 0.1 M_{\odot}$ star with unambiguous mass measurements. Bond et al. (2017) and Shvartzvald et al. (2017) detected a $q \sim 6 \times 10^{-5}$ planet in the microlensing event OGLE-2016-BLG-1195, and a joint analysis of ground-based and *Spitzer* data (Shvartzvald et al. 2017) revealed that this planetary system is composed of an Earth-mass ($\sim 1.4 M_{\oplus}$) planet around a $\sim 0.078 M_{\odot}$ ultracool dwarf. Han et al. (2013) discovered a $\sim 2 M_J$ planet orbiting a $\sim 0.02 M_{\odot}$ very low-mass brown dwarf (BD) in the event OGLE-2012-BLG-0358, and Bennett et al. (2008) detected a $\sim 3 M_{\oplus}$ super-Earth planet around a $\sim 0.08 M_{\odot}$ ultracool dwarf (Kubas et al. 2012) in the event MOA-2007-BLG-192. For the planets using Bayesian analysis to estimate the host mass, Jung et al. (2018a) reported a super-Jovian planet orbiting an $M_{\text{host}} < 0.1 M_{\odot}$ star with a $\sim 90\%$ probability. Jung et al. (2018b) reported a Jovian-mass planet around a BD, but the host star also has a $\sim 30\%$ probability to be an M dwarf or K-dwarf. In addition, there are three events with degenerate solutions. Bayesian analysis shows that one of the solutions of MOA-2015-BLG-337 (Miyazaki et al. 2018) and KMT-2016-BLG-1107 (Hwang et al. 2019) probably consist of a giant planet orbiting a BD. Sumi et al. (2016) found three degenerate planetary models in the event MOA-2013-BLG-605, two of which suggest a super-Earth orbiting a BD. For the five events using Bayesian analysis to estimate the host mass and/or that have degenerate solutions, we can verify that the host is an ultracool dwarf by adaptive-optics (AOs) instruments in the future.

Here, we report the analysis of the microlens planetary event OGLE-2015-BLG-1771. The observed data are consistent with three planetary models, and a Bayesian analysis suggests the host star is likely an ultracool dwarf ($M_{\text{host}} < 0.2 M_{\odot}$). The paper is structured as follows. In Section 2, we introduce data acquisition and processing of this event. We then describe the light-curve analysis in Section 3 and estimate the physical parameters of the planetary system in Section 4. Finally, we discuss the implications of our work in Section 5.

2. Observations

OGLE-2015-BLG-1771 was discovered by the Optical Gravitational Lensing Experiment (OGLE; Udalski et al. 2015) using its 1.3 m Warsaw Telescope at the Las Campanas Observatory in Chile and alerted by the OGLE Early Warning System (Udalski et al. 1994; Udalski 2003) at UT 00:46 on 2015 August 2. The event was located at equatorial coordinates $(\alpha, \delta)_{J2000} = (17:55:11.76, -28:51:45.9)$, corresponding to Galactic coordinates $(\ell, b) = (1.14, -1.76)$. It therefore lies in OGLE field BLG505, monitored by OGLE with a cadence of $\Gamma = 3 \text{ hr}^{-1}$. The event was also observed by the Korea Microlensing Telescope Network (KMTNet; Kim et al. 2016). KMTNet consists of three 1.6 m telescopes, equipped with 4

deg^2 field-of-view cameras at the Cerro Tololo Interamerican Observatory (CTIO) in Chile (KMTC), the South African Astronomical Observatory (SAAO) in South Africa (KMTS), and the Siding Spring Observatory (SSO) in Australia (KMTA). The event was located in the KMTNet BLG02 field, which was observed in 2015 with a cadence of $\Gamma = 6 \text{ hr}^{-1}$. The majority of observations by OGLE and KMTNet were taken in the *I*-band, with some *V*-band images taken for the color measurement of microlens sources. For the light-curve analysis, the *I*-band magnitude is instrumental magnitude, but the difference to the standard *I*-band magnitude is within 0.2 mag (Udalski et al. 2015). During $7230 < \text{HJD}' < 7237$ ($\text{HJD}' = \text{HJD} - 2450000$), the Moon was < 70 deg away from the target and the sky background was brighter than $V = 20 \text{ mag arcsec}^{-2}$, while the target was only $V \sim 22 \text{ mag}$ during the peak. Thus, the *V*-band data have a signal-to-noise ratio (S/N) too low to determine the source color. The photometry of OGLE and KMTNet was extracted using custom implementations of the difference image analysis technique (Alard & Lupton 1998): Wozniak (2000; OGLE) and Albrow et al. (2009; KMTNet).

3. Light-curve Analysis

Figure 1 shows the observed data together with the best-fit models. The light curve shows a “U” shape bump at $\text{HJD}' \sim 7235.1$, which is generally produced by a caustic crossing in a binary-lensing (2L1S) event, so we fit the data with the 2L1S model in Section 3.1. We also check the binary-source (1L2S) model in Section 3.2.

3.1. Binary-lens Model

Standard binary lens models require seven parameters to calculate the magnification, $A(t)$. The first three are point-lens parameters (t_0, u_0, t_E ; Paczyński 1986): the time at which the source passes closest to the center of lens mass, the impact parameter normalized by the angular Einstein radius θ_E , and the Einstein radius crossing time, respectively. The next three (q, s, α) define the binary companion: the mass ratio, the projected separation between the binary components scaled to θ_E , and the angle between the source trajectory and the binary axis in the lens plane, respectively. The last one ρ is the angular source radius θ_* scaled to θ_E ($\rho = \theta_*/\theta_E$). We use the advanced contour integration code (Bozza 2010), `VBBinaryLensing`,²⁰ to compute the binary-lens magnification $A(t)$. In addition, for each data set i , we introduce two flux parameters ($f_{S,i}, f_{B,i}$) to represent the flux of the source star and any additional blend flux. The observed flux, $f_i(t)$, calculated from the model, is

$$f_i(t) = f_{S,i}A(t) + f_{B,i}. \quad (1)$$

We locate the χ^2 minima by searching over a grid of parameters ($\log s, \log q, \alpha, \rho$). The grids consist of 41 values equally spaced between $-1 \leq \log s \leq 1$, 10 values equally spaced between $0^\circ \leq \alpha < 360^\circ$, 51 values equally spaced between $-5 \leq \log q \leq 0$ and 8 values equally spaced between $-3 \leq \log \rho \leq -1$. For each set of ($\log s, \log q, \alpha, \rho$), we fix $\log q, \log s$ and ρ , but free t_0, u_0, t_E, α . We find the minimum χ^2 by Markov chain Monte Carlo (MCMC) χ^2 minimization using the `emcee` ensemble sampler (Foreman-Mackey et al. 2013). The upper panel of Figure 2 shows the χ^2 distribution in the ($\log s, \log q$) plane from the grid search, which indicates

²⁰ <http://www.fisica.unisa.it/GravitationAstrophysics/VBBinaryLensing.htm>

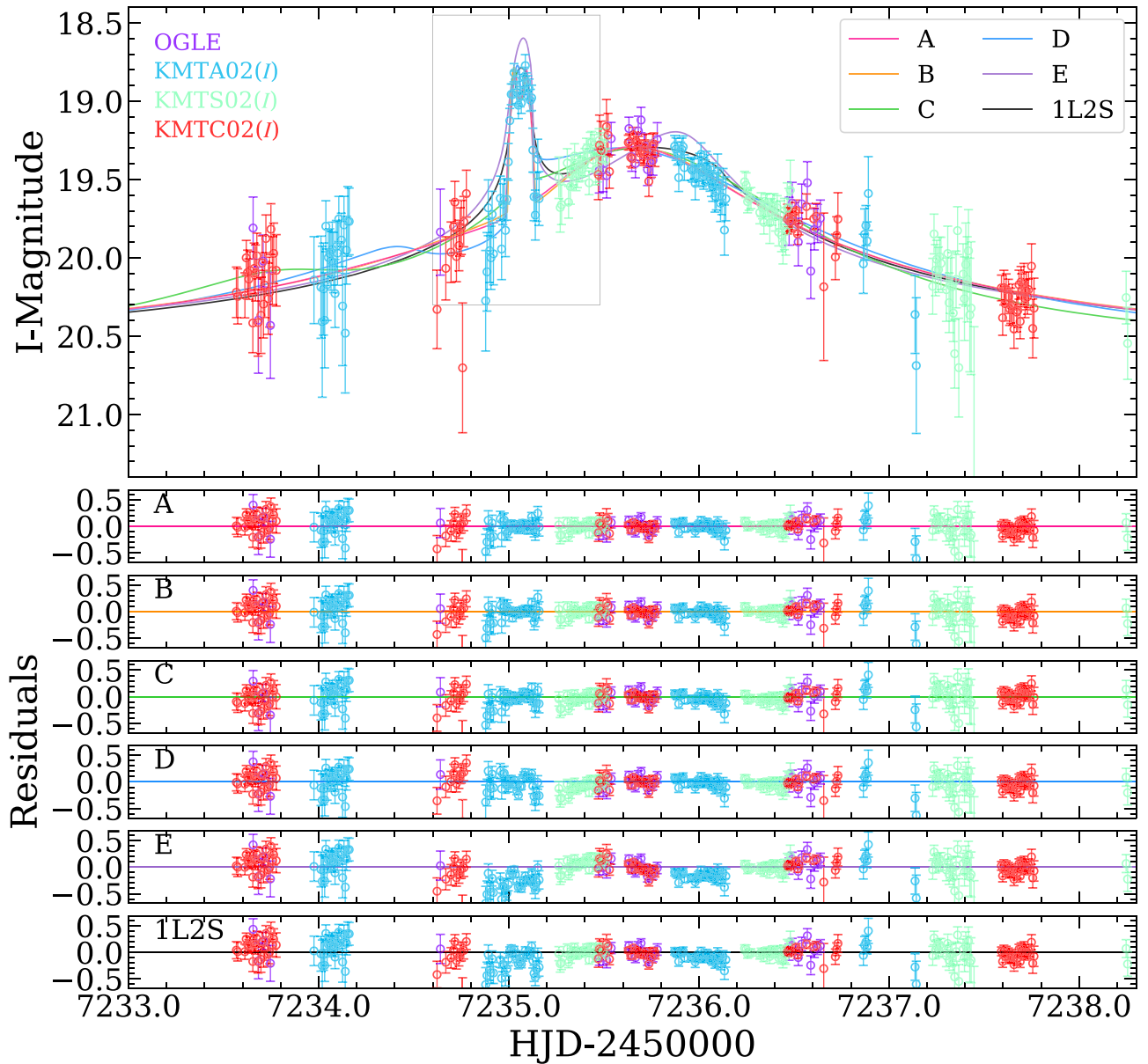


Figure 1. The data of OGLE-2015-BLG-1771 together with the best-fit 2L1S and 1L2S models. Data points for different data sets and light curves for different models are shown with different colors.

(The data used to create this figure are available.)

that the distinct minima are within $-0.5 \leq \log s \leq 0.5$ and $-4 \leq \log q \leq -1$. We therefore conduct a denser grid search, which consists of 101 values equally spaced between $-0.5 \leq \log s \leq 0.5$, 10 values equally spaced between $0^\circ \leq \alpha < 360^\circ$, and 41 values equally spaced between $-4 \leq \log q \leq 0$. As shown in the lower panel of Figure 2, we find five distinct minima (labeled as “A,” “B,” “C,” “D,” and “E” in the lower panel Figure 2).

We then investigate the best-fit model with all parameters set free using MCMC. The MCMC results show that the Model “A” provides the best fit to the observed data, while the Models “B,” “C,” “D,” and “E” are disfavored by $\Delta\chi^2 \sim 3, 15, 54,$ and $134,$ respectively (see Table 1 for the parameters and

their 68% uncertainty range from MCMC). Figure 3 shows the lens-system configurations of the individual degenerate models. In Figures 4 and 5, we find that most of the χ^2 difference of Models “D” and “E” are from the anomalous region. Together with the relatively large $\Delta\chi^2$, we only investigate Models “A,” “B,” and “C” in the following analysis. In addition, all of the surviving models (A, B, and C) have very low mass ratios, indicating that the companion is a planetary-mass object.

In some cases, the microlens parallax π_E can be measured by considering the orbital motion of Earth around the Sun in the light-curve analysis (Gould 1992; Alcock et al. 1995). However, this method is generally feasible only for events with long timescales $t_E \gtrsim \text{year}/2\pi$ (e.g., Udalski et al. 2018)

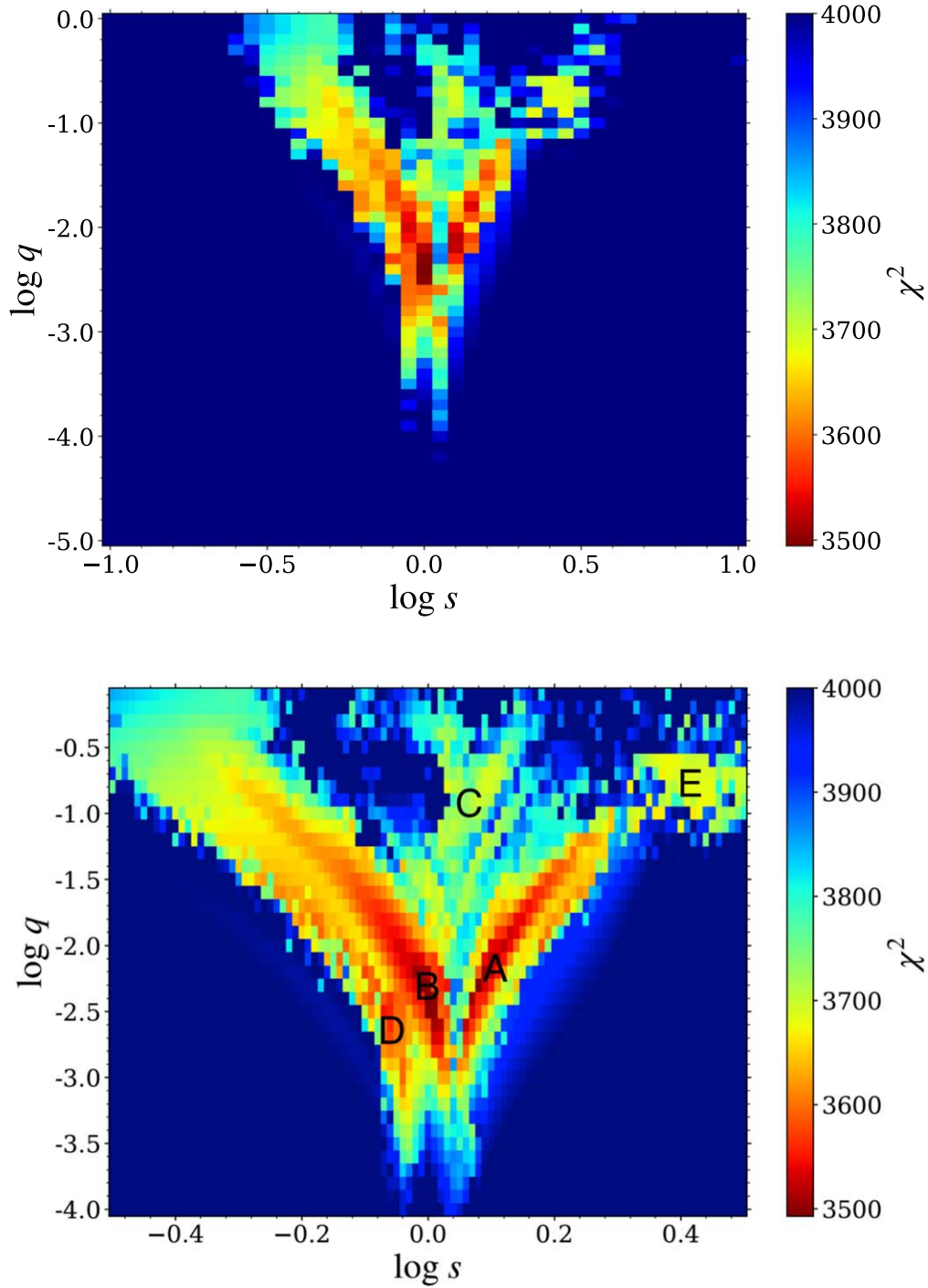


Figure 2. χ^2 distributions of the grid search projected onto the $(\log s, \log q)$ plane. The upper panel shows the space that is equally divided on a (41×51) grid with ranges of $-1.0 \leq \log s \leq 1.0$ and $-5.0 \leq \log q \leq 0$, respectively. The lower panel shows the space that is equally divided on a (101×41) grid with ranges of $-0.5 \leq \log s \leq 0.5$ and $-4.0 \leq \log q \leq 0$, respectively. The labels “A,” “B,” “C,” “D,” and “E” in the lower panel represent five distinct minima.

that introduce significant deviation from rectilinear motion in the lens-source relative motion. For OGLE-2015-BLG-1771, the timescale $t_E < 5$ days, so the parallax effect should be negligible. As a result, the addition of parallax to the models only provides $\Delta\chi^2 < 2$, and the upper limit of the microlens parallax as the 1σ level is $\pi_E \lesssim 100$ for all three models. The microlens parallax should be < 10 for typical microlensing events (see Table 2 of Zhu et al. 2017), so the light-curve analysis gives no useful constraint on the microlens parallax.

3.2. Binary-source Model

A binary-source event is the superposition of two point-lens events. Gaudi (1998) first pointed out that a 1L2S event can mimic a 2L1S event if the binary source (labeled as “S1” and “S2”) has a large flux ratio $q_F = f_{S1}/f_{S2}$ and the second source “S2” passes much closer to the lens. We therefore search for 1L2S solutions using MCMC, which shows that the best-fit 1L2S model is disfavored by $\Delta\chi^2 \sim 86$ compared to the best-

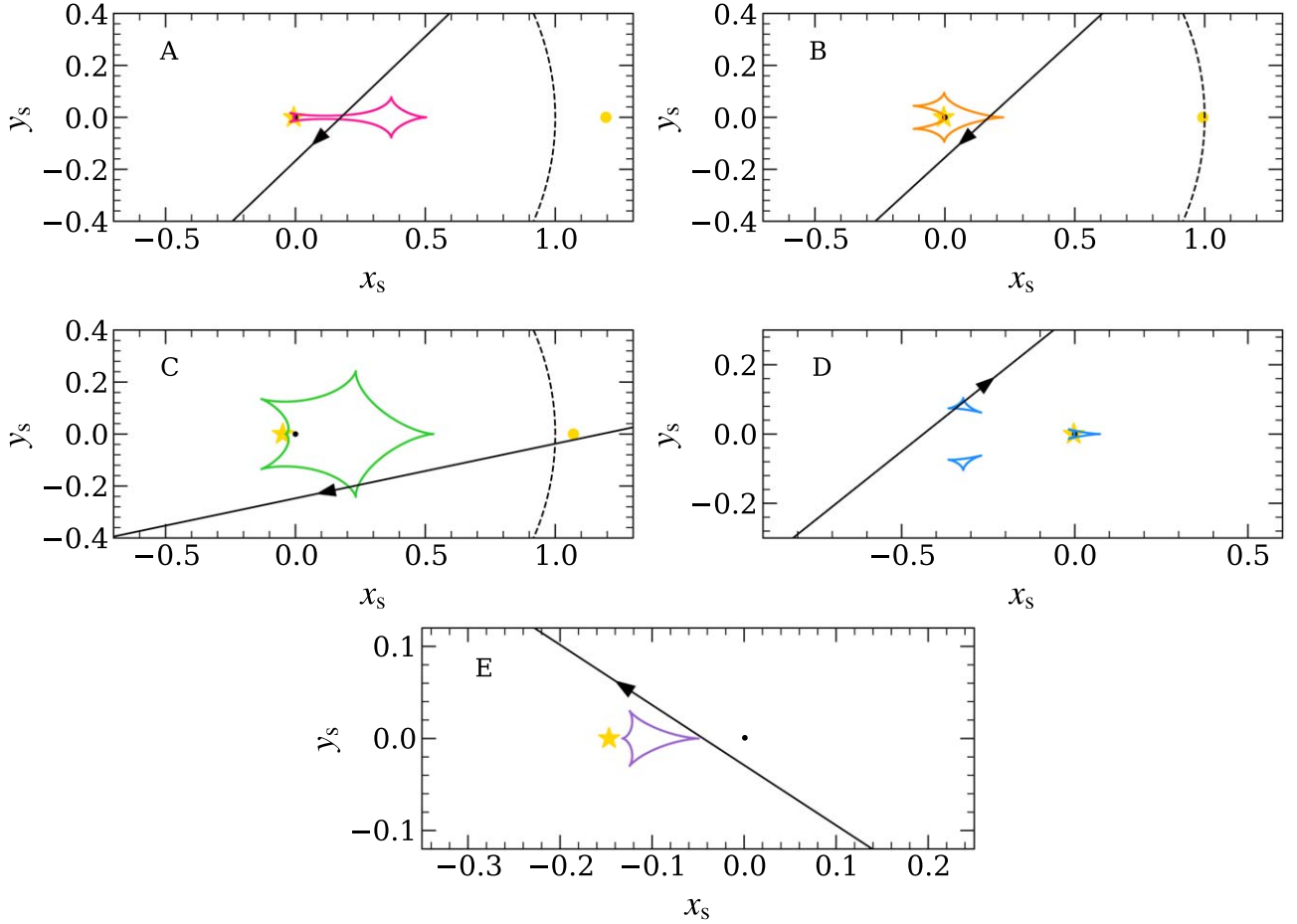


Figure 3. Geometries of the five different binary-lens models. In each panel, the caustic is color-coded to match the light curves in Figures 1 and 4. The yellow dots represent the positions of the planet, and the yellow asterisks represent the positions of the host star. The black solid line is the trajectory of the source, and the arrow indicates the direction of the source motion. The axes are in units of the Einstein radius θ_E , and the black dashed line is the angular Einstein ring of the lens system.

Table 1
Best-fit Models and Their 68% Uncertainty Range from MCMC

Models	A	B	C	D	E	Binary Source
$t_{0,1}$ (HJD')	7235.60 ± 0.01	7235.62 ± 0.01	7235.51 ± 0.01	7235.61 ± 0.01	7234.74 ± 0.23	7235.77 ± 0.02
$t_{0,2}$ (HJD')	7235.06 ± 0.03
$u_{0,1}$	0.121 ± 0.008	0.114 ± 0.006	0.242 ± 0.009	0.273 ± 0.016	0.024 ± 0.016	0.112 ± 0.024
$u_{0,2}$	0.001 ± 0.025
t_E (days)	4.28 ± 0.24	4.53 ± 0.18	2.49 ± 0.10	2.62 ± 0.12	8.64 ± 0.98	5.39 ± 0.85
s	1.202 ± 0.010	0.998 ± 0.008	1.119 ± 0.006	0.850 ± 0.008	2.216 ± 0.090	...
q (10^{-3})	5.38 ± 0.64	4.47 ± 0.51	45.5 ± 4.5	3.39 ± 0.35	70.9 ± 9.8	...
α (deg)	223.7 ± 1.2	222.4 ± 0.4	191.9 ± 0.4	38.6 ± 0.4	146.8 ± 0.8	...
ρ_1 (10^{-3})	4.41 ± 0.46	3.64 ± 0.34	8.27 ± 0.80	9.15 ± 0.78	4.41 ± 0.50	131 ± 27
ρ_2 (10^{-3})	10 ± 2
q_F	0.080 ± 0.012
I_S	21.77 ± 0.08	21.86 ± 0.06	20.91 ± 0.05	20.82 ± 0.08	22.86 ± 0.13	22.25 ± 0.24
I_B	21.03 ± 0.04	20.99 ± 0.03	22.04 ± 0.14	22.36 ± 0.30	20.74 ± 0.02	20.85 ± 0.06
χ^2/dof	3489.8/3481	3492.7/3481	3505.1/3481	3543.5/3481	3624.1/3481	3575.4/3480

fit 2L1S model (see Table 1 for the parameters). In Figure 5, we find that most of the χ^2 difference comes from the anomalous region, in which the 1L2S model cannot fit the “U” shape of the anomalous region. Thus, we exclude the 1L2S solution.

4. Physical Parameters

Uniquely determining the total lens mass M_L and distance D_L requires two observables: the angular Einstein radius θ_E and

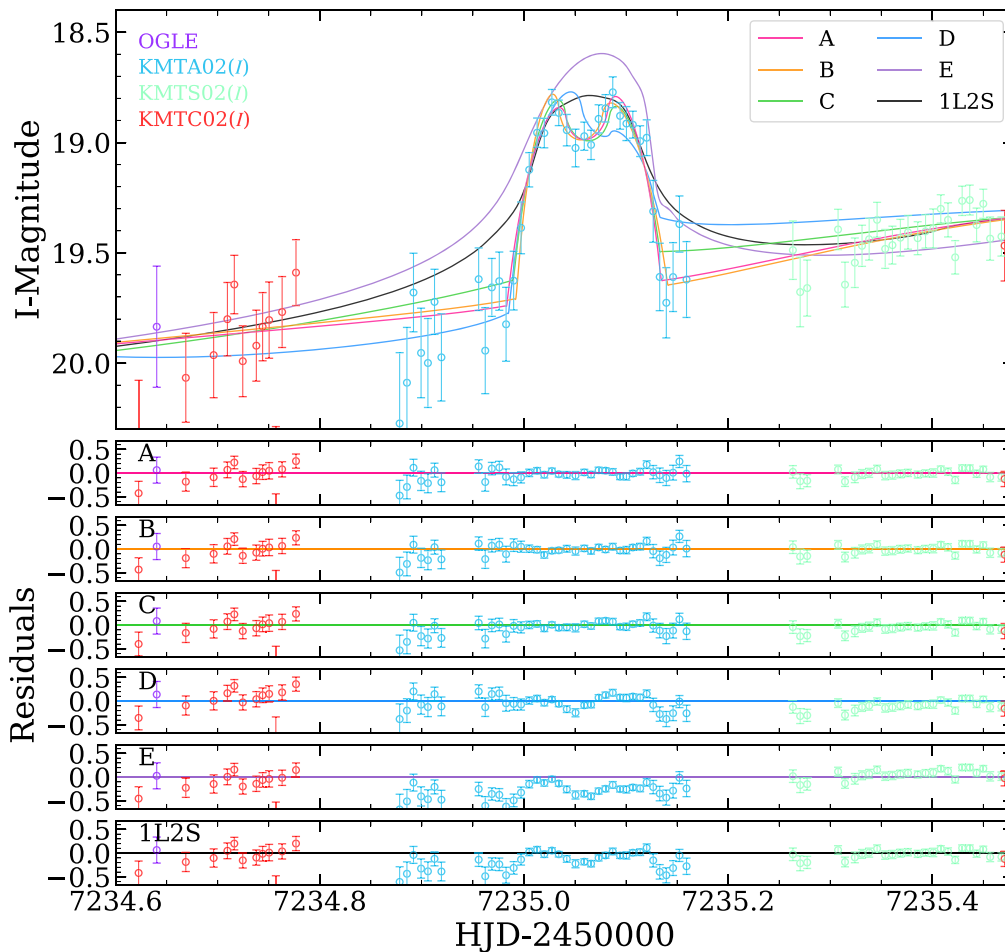


Figure 4. A zoom of the planetary anomaly region. The symbols are the same as those in Figure 1.

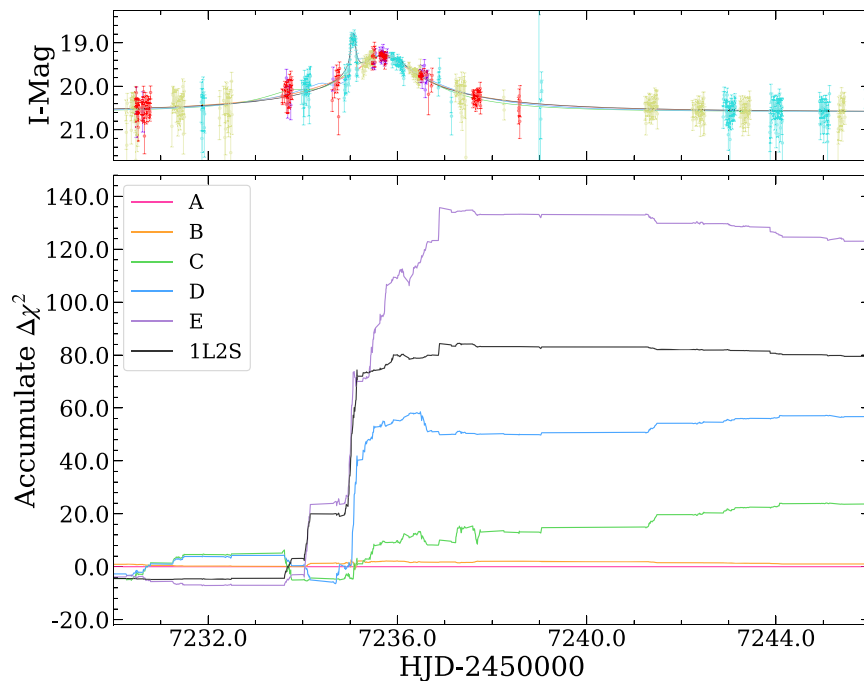


Figure 5. The upper panel shows the observed data with different models. The lower panel shows the cumulative distribution of χ^2 differences as a function of time between different models indicated by different colors. We use the 2L1S Model A as the reference model and the χ^2 differences are given by $\Delta\chi^2 = \chi^2_{\text{model}} - \chi^2_A$. Most of the χ^2 difference of 2L1S Models “D,” “E,” and 1L2S Model are from the anomalous region.

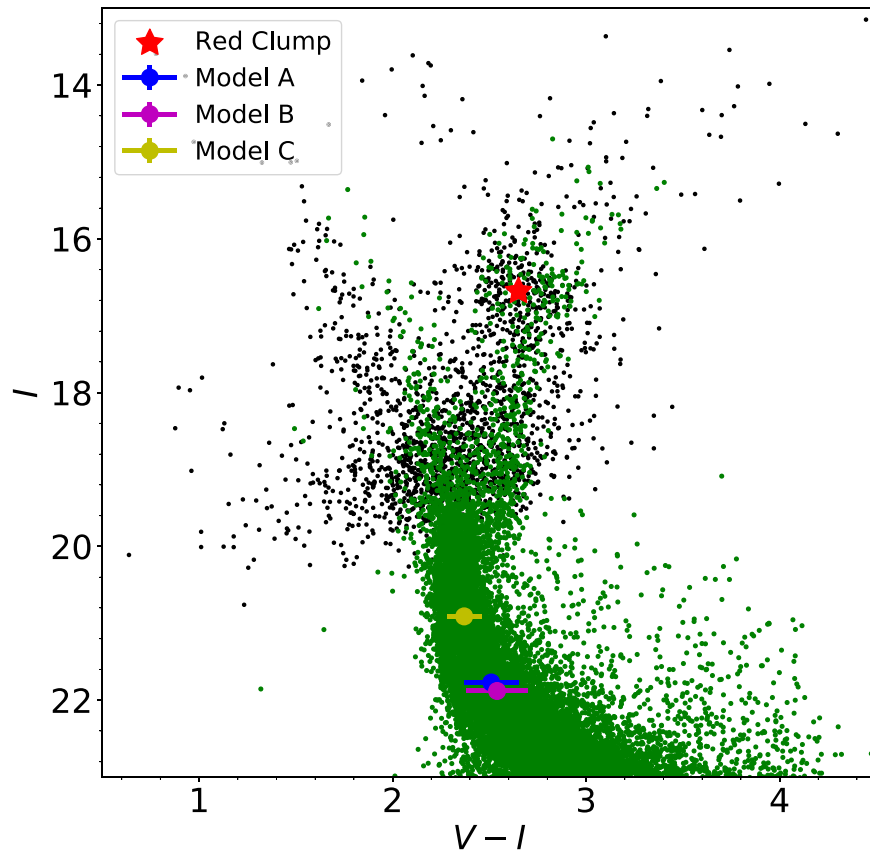


Figure 6. Color–magnitude diagram of a $2' \times 2'$ square centered on OGLE-2015-BLG-1771. The black dots show the stars from the OGLE catalog, which are roughly calibrated to the standard filter using the formula of Udalski et al. (2015). The green dots show the *HST* CMD of Holtzman et al. (1998) whose red-clump centroid is adjusted to OGLE’s using the Holtzman field red-clump centroid of $(V - I, I) = (1.62, 15.15)$; Bennett et al. 2008). The red asterisk shows the centroid of the red clump, and the blue, magenta, and yellow dots represent the position of the source of different models.

the microlens parallax π_E (Gould 1992, 2000)

$$M_L = \frac{\theta_E}{\kappa \pi_E}, \quad D_L = \frac{\text{au}}{\pi_E \theta_E + \pi_S}, \quad (2)$$

where $\kappa \equiv 4G/(c^2 \text{au}) = 8.144 \text{ mas}/M_\odot$, $\pi_S = \text{au}/D_S$ is the source parallax, and D_S is the source distance. We estimate the angular Einstein radius by $\theta_E = \theta_*/\rho$ in Section 4.1. However, the observed data give no useful constraint on the microlens parallax (see Section 3.1). Thus, we conduct a Bayesian analysis in Section 4.2 to estimate the physical parameters of the planetary system.

4.1. Color–Magnitude Diagram

We estimate the angular source radius θ_* based on the de-reddened brightness and color of the source (Yoo et al. 2004). We construct the color–magnitude diagram (CMD) using OGLE stars within a $2' \times 2'$ square centered on the position of the event (see Figure 6). We measure the centroid of the red giant clump as $(V - I, I)_{\text{cl}} = (2.65 \pm 0.01, 16.68 \pm 0.01)$, and compare it to the intrinsic centroid of the red giant clump $(V - I, I)_{\text{cl},0} = (1.06, 14.39)$; Bensby et al. 2013; Nataf et al. 2016), which yields an offset $\Delta(V - I, I)_{\text{cl}} = (1.59 \pm 0.02, 2.29 \pm 0.03)$.

From the light-curve modeling, the source apparent brightness is $I_{S,A} = 21.77 \pm 0.08$, $I_{S,B} = 21.86 \pm 0.06$ and $I_{S,C} = 20.91 \pm 0.05$ for Models “A,” “B,” and “C,” respectively. However, in this case, we have no color measurements of the

Table 2
De-reddened Source Color and Magnitude, the Values of θ_* , θ_E and μ_{rel}

Models	Unit	A	B	C
$I_{S,0}$	mag	19.48 ± 0.09	19.57 ± 0.07	18.62 ± 0.06
$(V - I)_{S,0}$	mag	0.92 ± 0.14	0.95 ± 0.16	0.78 ± 0.09
θ_*	μas	0.49 ± 0.08	0.48 ± 0.08	0.65 ± 0.07
θ_E	mas	0.111 ± 0.022	0.132 ± 0.025	0.079 ± 0.011
μ_{rel}	mas yr^{-1}	9.5 ± 2.0	10.6 ± 2.1	11.6 ± 1.7

source due to too low S/N in *V*-band. Nevertheless, it is still possible to estimate the source color following the method of Bennett et al. (2008) and Kondo et al. (2019). We first calibrate the CMD of Holtzman et al. (1998) *Hubble Space Telescope* (*HST*) observations to the OGLE CMD using its red-clump centroid of $(V - I, I)_{\text{cl},HST} = (1.62, 15.15)$ (Bennett et al. 2008). We then estimate the source color by taking the average color of the calibrated Holtzman field stars whose brightness are within 3σ of the microlens source star. Using the derived offset of the red giant clump, the de-reddened brightness $I_{S,0}$ and color $(V - I)_{S,0}$ of the source can be measured. Finally, we apply the color/surface-brightness relation of Adams et al. (2018) to estimate the angular source radius θ_* . We summarize the values of the source and the derived angular Einstein radius θ_E and the lens-source relative proper motion μ_{rel} in Table 2.

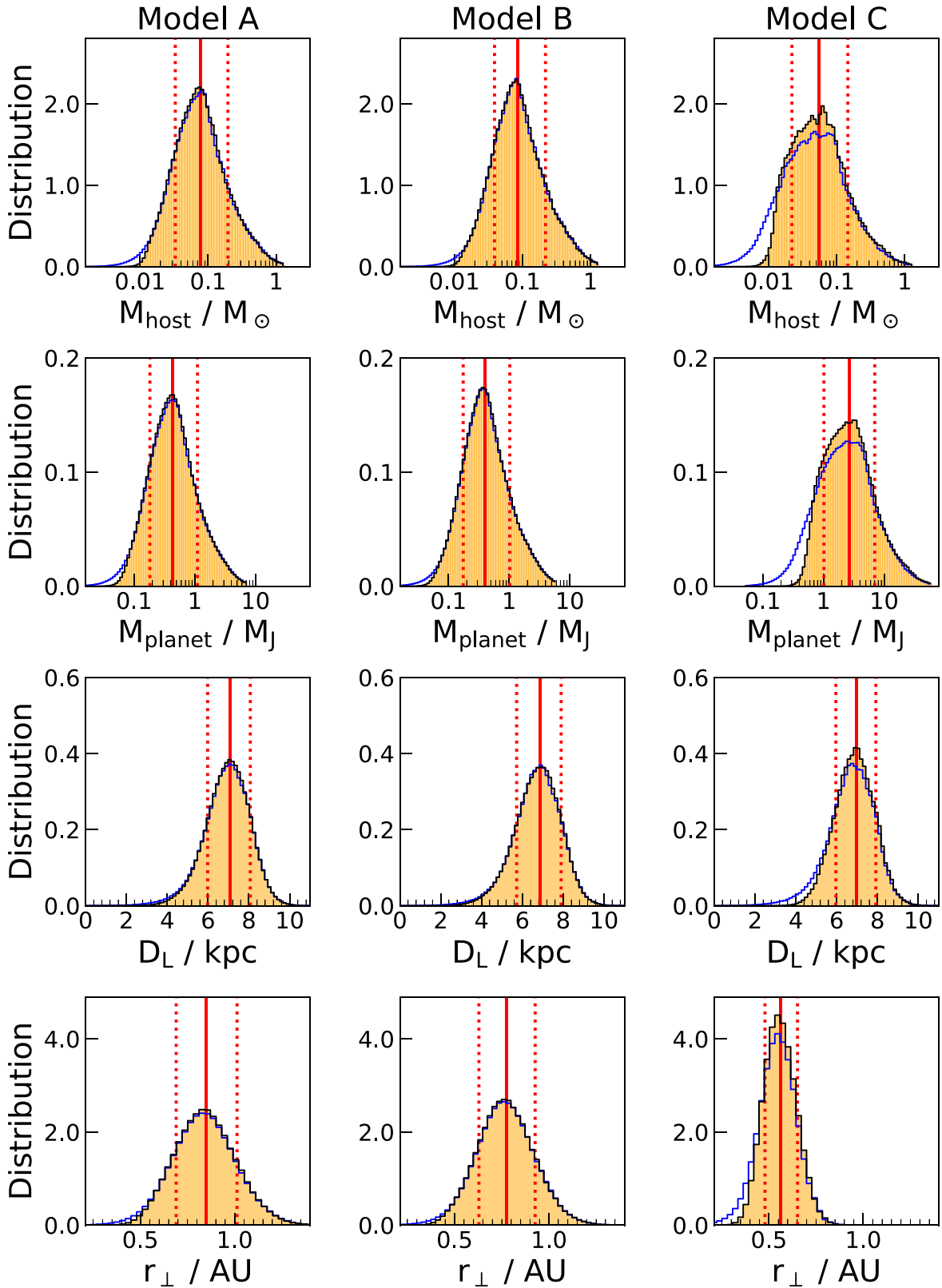


Figure 7. Bayesian posterior distributions of the lens host mass M_{host} , the lens distance D_{L} , the planet mass M_{planet} , and the projected planet-host separation r_{\perp} for Models “A,” “B,” and “C.” In each panel, the distributions marked in black are obtained with $\alpha_{\text{pl}} = -4.0$, while those marked in blue are derived with $\alpha_{\text{pl}} = 0.6$. The red solid vertical line and the two red dashed lines represent the median value and the 16th and 84th percentiles of the distribution obtained with $\alpha_{\text{pl}} = -4.0$.

Table 3
Physical Parameters for OGLE-2015-BLG-1771

Lens Parameters	Unit	$\alpha_{\text{pl}} = -4.0$			$\alpha_{\text{pl}} = 0.6$		
		Model A	Model B	Model C	Model A	Model B	Model C
M_{host}	M_{\odot}	$0.077^{+0.119}_{-0.044}$	$0.086^{+0.133}_{-0.047}$	$0.055^{+0.091}_{-0.033}$	$0.076^{+0.119}_{-0.044}$	$0.085^{+0.132}_{-0.047}$	$0.049^{+0.091}_{-0.033}$
M_{planet}	M_{J}	$0.433^{+0.674}_{-0.251}$	$0.401^{+0.624}_{-0.226}$	$2.634^{+4.361}_{-1.615}$	$0.427^{+0.672}_{-0.255}$	$0.397^{+0.620}_{-0.227}$	$2.331^{+4.368}_{-1.576}$
D_{L}	kpc	$7.07^{+1.00}_{-1.09}$	$6.86^{+1.04}_{-1.14}$	$6.96^{+0.96}_{-1.00}$	$7.04^{+1.02}_{-1.14}$	$6.83^{+1.05}_{-1.17}$	$6.85^{+1.02}_{-1.15}$
r_{\perp}	au	$0.85^{+0.16}_{-0.16}$	$0.78^{+0.15}_{-0.15}$	$0.56^{+0.09}_{-0.08}$	$0.85^{+0.16}_{-0.17}$	$0.77^{+0.15}_{-0.15}$	$0.55^{+0.09}_{-0.10}$
θ_{E}	mas	$0.100^{+0.019}_{-0.018}$	$0.114^{+0.021}_{-0.020}$	$0.072^{+0.010}_{-0.010}$	$0.100^{+0.019}_{-0.018}$	$0.115^{+0.021}_{-0.021}$	$0.071^{+0.010}_{-0.010}$
μ_{rel}	mas yr ⁻¹	$8.5^{+1.6}_{-1.5}$	$9.2^{+1.7}_{-1.6}$	$10.4^{+1.4}_{-1.4}$	$8.5^{+1.6}_{-1.5}$	$9.2^{+1.7}_{-1.6}$	$10.4^{+1.4}_{-1.4}$

4.2. Bayesian Analysis

Our Bayesian analysis is based on the Galactic model of Jung et al. (2018b) derived from the models of Han & Gould (1995, 2003). Because the timescale of the event is <5 days, we expect that objects in the planetary-mass regime are also plausible lenses (e.g., Miyazaki et al. 2018). We therefore adopt a broken power-law mass function as follows:

$$dN/dM = a_0 M^{-\alpha_{\text{pl}}} \quad (0.001 \leq M/M_{\odot} \leq 0.013) \quad (3)$$

$$dN/dM = a_1 M^{-0.3} \quad (0.013 \leq M/M_{\odot} \leq 0.08) \quad (4)$$

$$dN/dM = a_2 M^{-1.3} \quad (0.08 \leq M/M_{\odot} \leq 0.5) \quad (5)$$

$$dN/dM = a_3 M^{-2.3} \quad (0.5 \leq M/M_{\odot} \leq 1.3) \quad (6)$$

where the last three terms are the Kroupa mass function (Kroupa 2001) used in Zhu et al. (2017), (a_0, a_1, a_2, a_3) are normalizing coefficients, and α_{pl} is the slope of the planetary-mass regime. We create a sample of 10^9 simulated events for $\alpha_{\text{pl}} = -4.0$ and 0.6 , respectively. The planetary slope $\alpha_{\text{pl}} = -4.0$ is similar to that of Mróz et al. (2017) for unbound or wide-orbit Jupiter-mass planets. $\alpha_{\text{pl}} = 0.6$ has 1 : 0.26 for the relative fractions of number between main-sequence stars and planetary-mass objects, which is just slightly higher than the result of Mróz et al. (2017) who found that the upper limit on the frequency of Jupiter-mass free-floating or wide-orbit planets is 0.25 per main-sequence star at 95% confidence. For each simulated event i of model k , the weight is given by

$$W_{\text{Gal},i,k} = \Gamma_{i,k} \mathcal{L}_{i,k}(t_{\text{E}}) \mathcal{L}_{i,k}(\theta_{\text{E}}), \quad (7)$$

where $\Gamma_{i,k} \propto \theta_{\text{E},i,k} \times \mu_{\text{rel},i,k}$ is the microlensing event rate, $\mathcal{L}_{i,k}(t_{\text{E}})$ and $\mathcal{L}_{i,k}(\theta_{\text{E}})$ are the likelihood of its derived parameters ($t_{\text{E}}, \theta_{\text{E}}$) $_{i,k}$ given the error distributions of these quantities for that model

$$\mathcal{L}_{i,k}(X) = \frac{\exp[-(X_i - X_k)^2 / 2\sigma_{X_k}^2]}{\sqrt{2\pi}\sigma_{X_k}}, \quad X = t_{\text{E}} \text{ or } X = \theta_{\text{E}}. \quad (8)$$

The resulting posterior distributions of the lens host mass M_{host} , the lens distance D_{L} , the planet mass M_{planet} , the projected planet-host separation r_{\perp} , the angular Einstein radius θ_{E} , and the lens-source relative proper motion μ_{rel} for Models ‘‘A,’’ ‘‘B,’’ and ‘‘C’’ are shown Figure 7 and Table 3. For each parameter, the uncertainties are the 68% probability range about the median of the probability distribution. For Models ‘‘A’’ and ‘‘B,’’ the effects of different α_{pl} are negligible, and the planetary system is probably composed of a Saturn-mass planet orbiting a late M dwarf. For Model ‘‘C,’’ the distributions of planetary host mass ($M_{\text{host}} < 13 M_{\text{J}}$) are different for the two

α_{pl} , with 3.2% probability distribution for $\alpha_{\text{pl}} = -4.0$ and 12.0% for $\alpha_{\text{pl}} = 0.6$. Because both distributions indicate a mid-mass BD host star, we adopt the distributions of $\alpha_{\text{pl}} = -4.0$ for the final lens properties. The projected planet-host separation is $\sim 0.5\text{--}1.0$ au for the three models, which indicates that the planet is well beyond the snow line (assuming a snow line radius $r_{\text{SL}} = 2.7(M/M_{\odot})$ au; Kennedy & Kenyon 2008).

5. Discussion



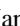

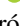

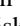
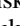
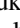
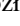

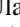

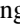
We have reported the discovery and analysis of the microlens planet OGLE-2015-BLG-1771Lb. Our analysis suggests that the planetary system probably consists of a gas-giant planet and an ultracool dwarf. This conclusion is based on a Bayesian analysis that shows that the lens has a $\sim 65\%$ probability of being $<0.1 M_{\odot}$ and a $\sim 85\%$ probability of being $<0.2 M_{\odot}$ (for $\alpha_{\text{pl}} = -4.0$). Of course, this still leaves a significant possibility that the lens could be a more massive star. For example, similar to this event, the Bayesian posterior for the primary of OGLE-2014-BLG-0962 (Shan et al. 2019) peaks at a mass of $\sim 0.07 M_{\odot}$ with an 84% probability that the mass is $<0.2 M_{\odot}$. However, including the parallax measurement for that event yields a measured mass of $0.2 M_{\odot}$. In the present case, the measured source-lens relative proper motion for the three models is quite large (see Table 2) and the source is quite faint ($I > 20.7$). This is similar to the case of OGLE-2005-BLG-169 for which *HST* (Bennett et al. 2015) was able to resolve the source and the lens when they were separated by ~ 48 mas. Thus, even for model A (which has the lowest proper motion, $\mu_{\text{rel}} \sim 8.5$ mas yr⁻¹), the source and lens will be separated by ~ 50 mas as soon as 2020. If the host star is an $M < 0.1 M_{\odot}$ star, the lens apparent magnitude should be $I \gtrsim 27$, which cannot be observed. Thus, we can verify within a few years that the host is an ultracool dwarf by excluding $M \gtrsim 0.1 M_{\odot}$ hosts for OGLE-2015-BLG-1771 using high-resolution imaging.

For many years (beginning with the second microlens planet, OGLE-2005-BLG-071Lb; Udalski et al. 2005), most microlensing planets were discovered based on the strategy advocated by Gould & Loeb (1992) using a combination of wide-area surveys for finding microlensing events and intensive follow-up observations for capturing the planetary perturbation. The second-generation microlensing surveys, conducted by the Microlensing Observations in Astrophysics (MOA; Sumi et al. 2016), OGLE, Wise Observatory (Shvartzvald et al. 2016), and KMTNet, aim to detect planets by wide-area, high-cadence observations, without the need for follow-up observations. For the planet OGLE-2015-BLG-1771Lb, the event timescale (<5 days) and the planetary signal (~ 5 hr) are short, and the anomaly is faint ($I_{\text{anom}} \sim 19$). Because the detection limit of the microlens follow-up

observations is $I \lesssim 18$ (Gould et al. 2010; Cassan et al. 2012), this planet can only be detected by the second-generation microlensing surveys. For those nine microlens planets that have a $>50\%$ probability to orbit an $M_{\text{host}} < 0.1 M_{\odot}$ host star, only OGLE-2012-BLG-0358Lb was detected using the strategy of Gould & Loeb (1992). Moreover, the rate of discovery of such planets is much higher beginning with 2015 (i.e., the observations of KMTNet), during which 6/9 planets were detected. In addition, the typical timescale t_E for the microlensing events with an $M < 0.1 M_{\odot}$ lens is $\lesssim 10$ days. For the three planets detected before 2015, all of them have $t_E > 20$ days, while 5/6 planets beginning with 2015 have $t_E < 10$ days, which suggests that the current second-generation microlensing surveys are more sensitive to the planets around ultracool dwarfs. Future statistical analyses of the microlens sample of planets around ultracool dwarfs will potentially reveal the properties of such planets and thus provide stringent constraints on the planet formation theories.

We thank Chris W. Ormel and Xuening Bai for fruitful discussions. X.Z., W.Z., W.T., H.Y., and S.M. acknowledge support by the National Science Foundation of China (grant No. 11821303 and 11761131004). The OGLE has received funding from the National Science Centre, Poland, grant MAESTRO 2014/14/A/ST9/00121 to AU. Work by A.G. was supported by AST-1516842 and by JPL grant 1500811. This research has made use of the KMTNet system operated by the Korea Astronomy and Space Science Institute (KASI) and the data were obtained at three host sites of CTIO in Chile, SAAO in South Africa, and SSO in Australia. A.G. received support from the European Research Council under the European Unions Seventh Framework Programme (FP 7) ERC grant Agreement No. [321035]. Work by C.H. was supported by the grants (2017R1A4A1015178 and 2019R1A2C2085965) of National Research Foundation of Korea. W.Z. was supported by the Beatrice and Vincent Tremaine Fellowship at CITA. This research has made use of the NASA Exoplanet Archive, which is operated by the California Institute of Technology, under contract with the National Aeronautics and Space Administration under the Exoplanet Exploration Program.

ORCID iDs

Weicheng Zang  <https://orcid.org/0000-0001-6000-3463>
 Yoon-Hyun Ryu  <https://orcid.org/0000-0001-9823-2907>
 Hongjing Yang  <https://orcid.org/0000-0003-0626-8465>
 Shude Mao  <https://orcid.org/0000-0001-8317-2788>
 Przemek Mróz  <https://orcid.org/0000-0001-7016-1692>
 Jan Skowron  <https://orcid.org/0000-0002-2335-1730>
 Igor Soszyński  <https://orcid.org/0000-0002-7777-0842>
 Paweł Pietrukowicz  <https://orcid.org/0000-0002-2339-5899>
 Szymon Kozłowski  <https://orcid.org/0000-0003-4084-880X>
 Krzysztof Ulaczyk  <https://orcid.org/0000-0001-6364-408X>
 Michael D. Albrow  <https://orcid.org/0000-0003-3316-4012>
 Sun-Ju Chung  <https://orcid.org/0000-0001-6285-4528>
 Cheongho Han  <https://orcid.org/0000-0002-2641-9964>
 Kyu-Ha Hwang  <https://orcid.org/0000-0002-9241-4117>

Youn Kil Jung  <https://orcid.org/0000-0002-0314-6000>
 In-Gu Shin  <https://orcid.org/0000-0002-4355-9838>
 Yossi Shvartzvald  <https://orcid.org/0000-0003-1525-5041>
 Jennifer C. Yee  <https://orcid.org/0000-0001-9481-7123>
 Wei Zhu  <https://orcid.org/0000-0003-4027-4711>
 Richard W. Pogge  <https://orcid.org/0000-0003-1435-3053>

References

- Adams, A. D., Boyajian, T. S., & von Braun, K. 2018, *MNRAS*, 473, 3608
 Alard, C., & Lupton, R. H. 1998, *ApJ*, 503, 325
 Albrow, M. D., Horne, K., Bramich, D. M., et al. 2009, *MNRAS*, 397, 2099
 Alcock, C., Allsman, R. A., Alves, D., et al. 1995, *ApJL*, 454, L125
 Bennett, D. P., Bhattacharya, A., Anderson, J., et al. 2015, *ApJ*, 808, 169
 Bennett, D. P., Bond, I. A., Udalski, A., et al. 2008, *ApJ*, 684, 663
 Bensby, T., Yee, J. C., Feltzing, S., et al. 2013, *A&A*, 549, A147
 Bond, I. A., Bennett, D. P., Sumi, T., et al. 2017, *MNRAS*, 469, 2434
 Boss, A. P. 2006, *ApJ*, 643, 501
 Bozza, V. 2010, *MNRAS*, 408, 2188
 Cassan, A., Kubas, D., Beaulieu, J. P., et al. 2012, *Natur*, 481, 167
 Chauvin, G., Lagrange, A.-M., Dumas, C., et al. 2004, *A&A*, 425, L29
 Daemgen, S., Natta, A., Scholz, A., et al. 2016, *A&A*, 594, A83
 Foreman-Mackey, D., Hogg, D. W., Lang, D., & Goodman, J. 2013, *PASP*, 125, 306
 Gaudi, B. S. 1998, *ApJ*, 506, 533
 Gauza, B., Béjar, V. J. S., Pérez-Garrido, A., et al. 2015, *ApJ*, 804, 96
 Gillon, M., Triard, A. H. M. J., Demory, B.-O., et al. 2017, *Natur*, 542, 456
 Gould, A. 1992, *ApJ*, 392, 442
 Gould, A. 2000, *ApJ*, 542, 785
 Gould, A., Dong, S., Gaudi, B. S., et al. 2010, *ApJ*, 720, 1073
 Gould, A., & Loeb, A. 1992, *ApJ*, 396, 104
 Han, C., & Gould, A. 1995, *ApJ*, 447, 53
 Han, C., & Gould, A. 2003, *ApJ*, 592, 172
 Han, C., Jung, Y. K., Udalski, A., et al. 2013, *ApJ*, 778, 38
 Holtzman, J. A., Watson, A. M., Baum, W. A., et al. 1998, *AJ*, 115, 1946
 Hwang, K.-H., Ryu, Y.-H., Kim, H.-W., et al. 2019, *AJ*, 157, 23
 Ida, S., & Lin, D. N. C. 2005, *ApJ*, 626, 1045
 Jung, Y. K., Hwang, K.-H., Ryu, Y.-H., et al. 2018a, *AJ*, 156, 208
 Jung, Y. K., Udalski, A., Gould, A., et al. 2018b, *AJ*, 155, 219
 Kennedy, G. M., & Kenyon, S. J. 2008, *ApJ*, 673, 502
 Kim, S.-L., Lee, C.-U., Park, B.-G., et al. 2016, *JKAS*, 49, 37
 Kondo, I., Sumi, T., Bennett, D. P., et al. 2019, *AJ*, 158, 224
 Kroupa, P. 2001, *MNRAS*, 322, 231
 Kubas, D., Beaulieu, J. P., Bennett, D. P., et al. 2012, *A&A*, 540, A78
 Liu, M. C., Delorme, P., Dupuy, T. J., et al. 2011, *ApJ*, 740, 108
 Mao, S., & Paczynski, B. 1991, *ApJL*, 374, L37
 Miyazaki, S., Sumi, T., Bennett, D. P., et al. 2018, *AJ*, 156, 136
 Mróz, P., Udalski, A., Skowron, J., et al. 2017, *Natur*, 548, 183
 Nataf, D. M., Gonzalez, O. A., Casagrande, L., et al. 2016, *MNRAS*, 456, 2692
 Paczyński, B. 1986, *ApJ*, 304, 1
 Shan, Y., Yee, J. C., Udalski, A., et al. 2019, *ApJ*, 873, 30
 Shvartzvald, Y., Maoz, D., Udalski, A., et al. 2016, *MNRAS*, 457, 4089
 Shvartzvald, Y., Yee, J. C., Calchi Novati, S., et al. 2017, *ApJL*, 840, L3
 Sumi, T., Udalski, A., Bennett, D. P., et al. 2016, *ApJ*, 825, 112
 Testi, L., Natta, A., Scholz, A., et al. 2016, *A&A*, 593, A111
 Todorov, K., Luhman, K. L., & McLeod, K. K. 2010, *ApJL*, 714, L84
 Udalski, A. 2003, *AcA*, 53, 291
 Udalski, A., Jaroszyński, M., Paczyński, B., et al. 2005, *ApJL*, 628, L109
 Udalski, A., Ryu, Y.-H., Sajadian, S., et al. 2018, *AcA*, 68, 1
 Udalski, A., Szymanski, M., Kaluzny, J., et al. 1994, *AcA*, 44, 227
 Udalski, A., Szymański, M. K., & Szymański, G. 2015, *AcA*, 65, 1
 Wozniak, P. R. 2000, *AcA*, 50, 421
 Yoo, J., DePoy, D. L., Gal-Yam, A., et al. 2004, *ApJ*, 603, 139
 Zechmeister, M., Dreizler, S., Ribas, I., et al. 2019, *A&A*, 627, A49
 Zhu, W., Udalski, A., Calchi Novati, S., et al. 2017, *AJ*, 154, 210